www.sciencemag.org/cgi/content/full/332/6036/1396/DC1

Supporting Online Material for

EPOXI at Comet Hartley 2

Michael F. A'Hearn,* Michael J. S. Belton, W. Alan Delamere, Lori M. Feaga, Donald Hampton, Jochen Kissel, Kenneth P. Klaasen, Lucy A. McFadden, Karen J. Meech, H. Jay Melosh, Peter H. Schultz, Jessica M. Sunshine, Peter C. Thomas, Joseph Veverka, Dennis D. Wellnitz, Donald K. Yeomans, Sebastien Besse, Dennis Bodewits, Timothy J. Bowling, Brian T. Carcich, Steven M. Collins, Tony L. Farnham, Olivier Groussin, Brendan Hermalyn, Michael S. Kelley, Michael S. Kelley, Jian-Yang Li, Don J. Lindler, Carey M. Lisse, Stephanie A. McLaughlin, Frédéric Merlin, Silvia Protopapa, James E. Richardson, Jade L. Williams

*To whom correspondence should be addressed. E-mail: ma@astro.umd.edu

Published 17 June 2011, *Science* **332**, 1396 (2010)
DOI: 10.1126/science.1204054

This PDF file includes:

Supplementary On-line Material

Global Comparison

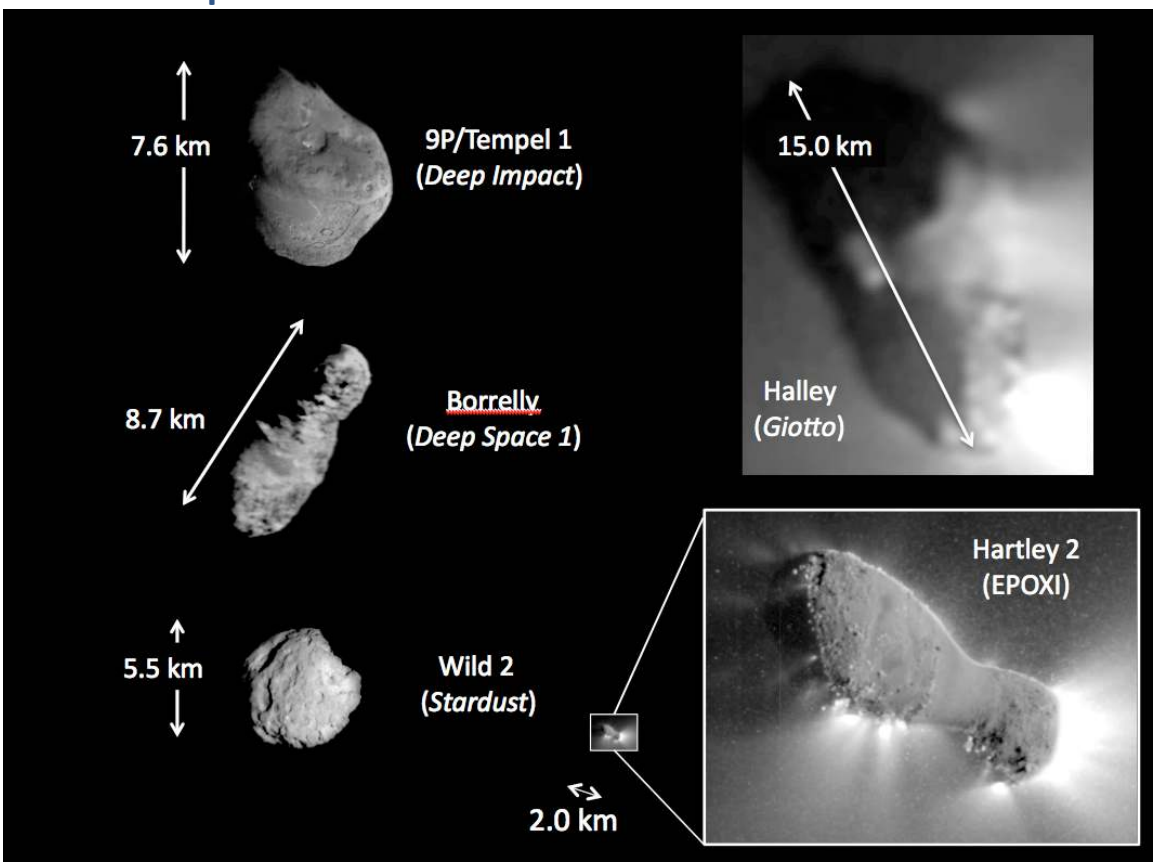

Figure S1. Images at the same scale for all cometary nuclei observed by spacecraft. Differences in overall shape are dramatic, as are the differences in contrast between the nuclei and their associated jets, which are brighter than the nucleus at Halley and Hartley 2 and much fainter than the nucleus at the other comets.

Rotational State

For background discussion of excited states of rotation in the context of small bodies see (*38-40*)**.** These references also include the background mathematical derivations. Our discussion is based on a Long Axis Mode (LAM) as described in those references since this is far more likely dynamically possible than a short-axis mode (SAM) based on the observed properties, including the observed axial ratios.

Periodogram analysis of the light curve on approach revealed seven periods in the earliest data, from E-60 to E-40 d (E = time of encounter), of which six are shown in Fig. S2. Subsequent accumulating data then showed that these periods were changing over the course of the encounter (Fig. S2). Periods P2 and P4 increase with time and are associated with the precession period of the long axis around the angular momentum

vector and its first sub-harmonic. Thus the period of precession of the long-axis is varying from <17 to >18 hours, with a value 18.34±0.04 h at encounter. The observed motion of the nucleus in the short interval over which the nucleus was clearly spatially resolved is consistent with P2 but not with P4 as the true precession period. Furthermore, the morphology of the coma as seen from ground-based telescopes also repeats approximately (but not exactly) with the period P2.

Periods P1, P3, P5, and P6 decrease with time and are associated with the roll around the long axis. We adopt P3 = 27.79±0.31 h at encounter as the roll period. P1 has very low power in the periodogram analysis and is therefore likely a harmonic, but P5 has power comparable to P3 and can not be excluded. Since the roll around the long axis has low linear speeds at the surface, the motion can not be seen in our resolved images. The ambiguity has no effect on any of our conclusions in this paper. The rates of change of the periods, determined from fitting a straight line to the data in Fig. S2, are given in Table S1. P7 is relatively weak, approximately 8×P2 and off scale in Fig. S2.

As a first approximation, the spatial orientation of the rotation state has been determined assuming that the end of the long axis traces out a great circle on the sky. This is equivalent to assuming that the rotation is not excited, a reasonable first approximation since our subsequent studies show that the excitation is small. We constrained the direction of the total angular momentum vector by the change in position angle of the projected axis of figure of the nucleus and its apparent length on approach to encounter. In a set of 11 resolved and deconvolved HRI images[1] from the last hour of approach, the actual orientation of the long axis moved over an 18° arc on the sky, which constrained the direction of the total Angular Momentum Vector (AMV) to RA, Dec = 17°± 11°, 47°± 2° in this approximation. At encounter (JD2455505.08318) the small, active end of the long axis points towards RA, Dec = 226.1°, 39.4° (± 0.7° circular error).

Although the roll period is still uncertain we conclude that the excitation is not extreme based on ratios of the principal moments of inertia obtained from the shape model assuming a homogeneous density distribution. Using the theory of force-free rigid body rotation (*39*), we find that the long axis should be inclined to the AMV by 80° to 84° and that any "nodding" motion of this axis should have an amplitude < 1°, too small to be detectable in our data. The excited spin state is still being evaluated and we expect that the excited solution will displace the orientation of the AMV by <~20°.

Weighted Trend-Line Parameters for 103P/Hartley 2				
	Frequency		Period	
#	Slope x 10^6 (hr^{-1}/dy)	Intercept (hr^{-1})	Slope x 10^3 (hr^{-1}/dy)	Intercept (hr)
f_1	+2 ± 17	0.0901 ± 0.0004	-0.5 ± 2	11.09 ± 0.05
f_2	-72 ± 7	0.0543 ± 0.0001	+24 ± 2	18.34 ± 0.04
f_3	+21 ± 17	0.0360 ± 0.0004	-17 ± 13	27.79 ± 0.31
f_4	-37 ± 3	0.0272 ± 0.0001	+49 ± 4	36.73 ± 0.08
f_5	+4 ± 2	0.0180 ± 0.00003	-5 ± 7	55.42 ± 0.10
f_6	+22 ± 5	0.0121 ± 0.0001	-165 ± 32	82.64 ± 0.57

Table S1. Weighted slopes in Figure S2. The intercepts represent our best estimates of the component periodicities at encounter. The form of the trend-line is y = slope · x+ y_0 where x is days from encounter and y_0 is the intercept at encounter (JD 2455505.08318).The number (#) of the periodicity is given in column 1 and shown in Figures S2 and S3.

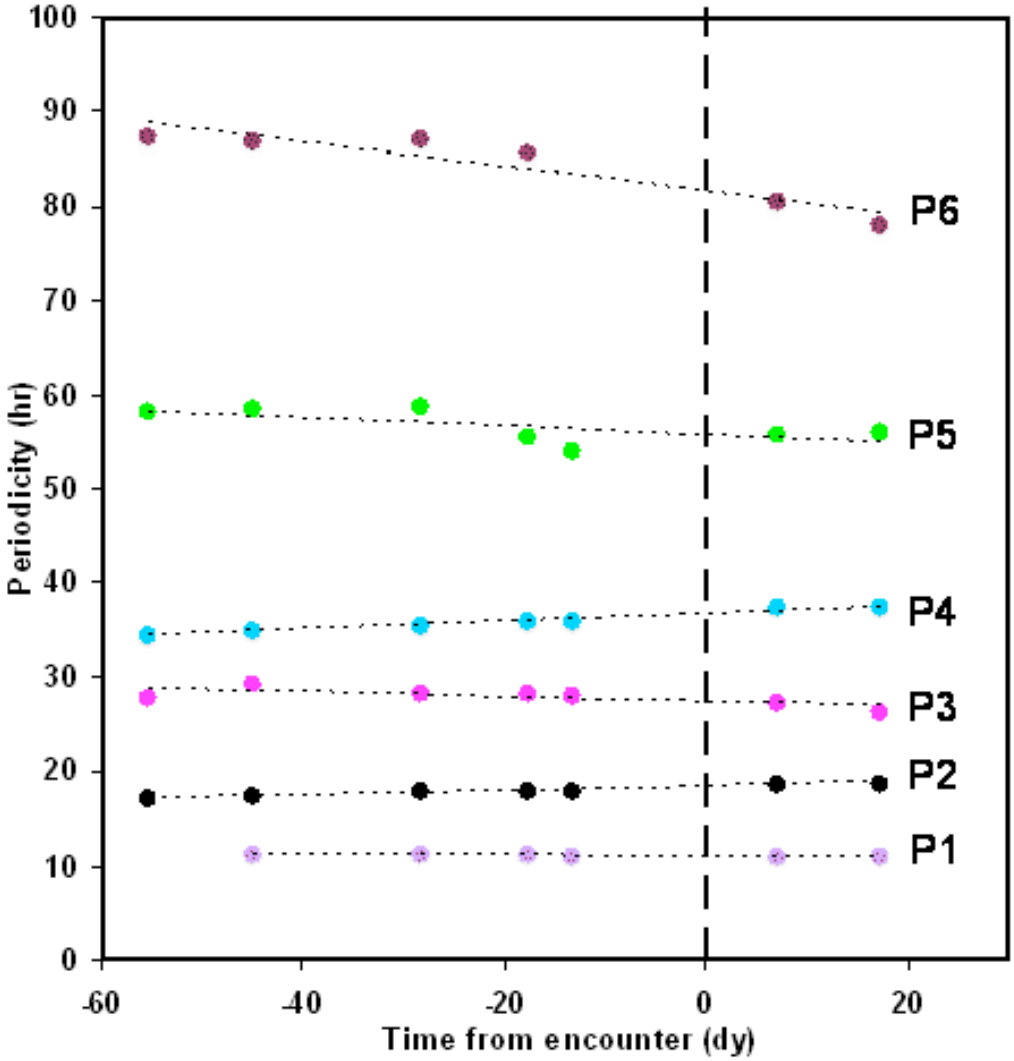

Figure S2. Variation of the periodicities seen in the light-curve of the comet through the EPOXI/DIXI encounter. The periodicities P2 and P4 increase with time (a third, longer period that increases with time, P7, is not shown here in order to increase the clarity of the presentation); the remaining periodicities, P1, P3, P5, and P6, decrease with time. We associate the former group with the precession of the long axis of the nucleus around the total angular momentum vector and the latter group with the spin component around the long axis.

Our estimates of the total angular momentum and total rotational energy per unit mass are ~1.1×10^5 m^2h^{-1} and ~2×10^4 m^2h^{-2} and these are changing at the rather substantial rates of ~0.1%/d and ~0.2 %/d, respectively. The change in rotational period (or angular momentum) of Tempel 1, for comparison, is ~0.02% per day near perihelion (*41*). The harmonic relationships between the periodicities are quite clear in the data with a strong first sub-harmonic of both the precession and roll periods appearing in the periodograms. The rapid change in the periods and the temporal changes in the non-gravitational acceleration of the comet in its orbit both are indicative of the combination

of a high outgassing rate coupled with a small mass and, for the periods, a very elongated shape. Figure S3 combines our data on the precessional period, P2, with a variety of other observations (*18, 42-45*) and shows that the precessional period remains constant while the comet is far from the sun and inactive but that it changes rapidly around perihelion while the comet is active. Finally, the precession and roll periods appear to be nearly commensurate (~2:3), but this is likely a coincidence since these periods are changing rapidly in opposite directions. Such commensurability has been seen before in the case of 1P/Halley (*39, 46*), where it is apparently a stable resonant phenomenon. It is a feature that has been seen in numerical simulations of the evolution of cometary spin (*47*).

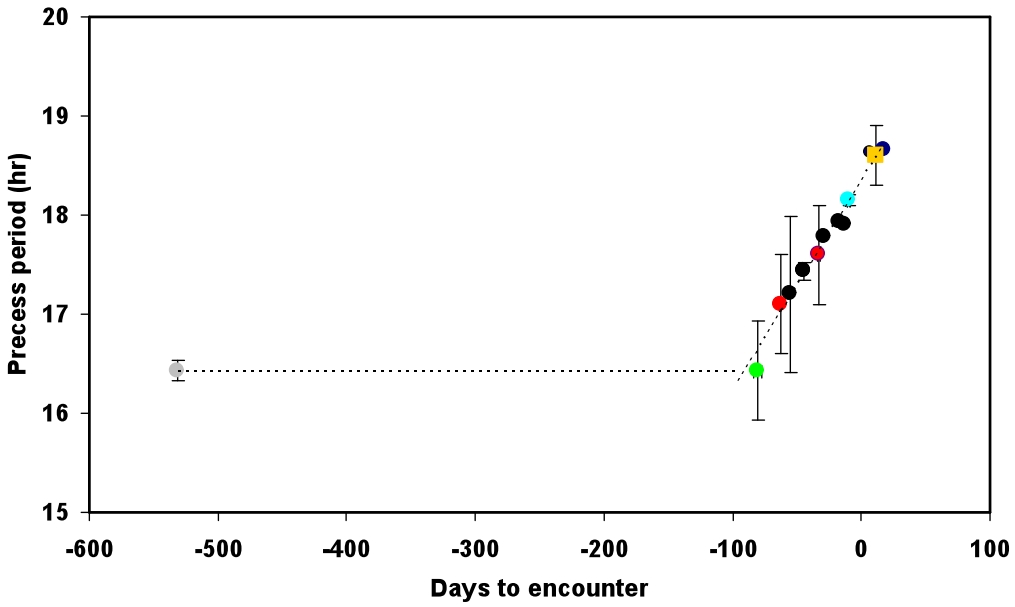

Figure S3. Change in the precessional period of the long axis around the total angular momentum vector as seen from the ground and from the *Deep Impact* spacecraft. Color code for ground-based observations: grey (*42*); aqua (*18*); red (*43*); gold (*44*); green (*45*). The seven EPOXI/DIXI points are in black.

[1] HRI Images used for determining the orientation of the AMV were hv5000005, hv5000022, hv5000065, hv5000095, hv5000118, hv5000139, hv5000152, hv5000152, hv5002000, hv5002015, hv5002028, and hv5002044.

Equipotential Surface

The equipotential model for the surface gravity was used to fit the shape of only the waist. We have not attempted to model the shape of the entire nucleus as an equipotential. The model for the potential includes the effect of the precession of the long axis around the Angular Momentum Vector but does not include the effect of the roll around the long axis. Because the period of roll is long and the lever-arm at the surface is short, the contribution of roll to the potential is unimportant. Figure S4 shows the normalized variance[1] between the observed shape and the calculated potential, in the

waist only, as a function of density. The minimum variance is at $\rho = 220$ kg m^{-3}, which corresponds to a total mass = 1.84×10^{11} kg. At that minimum, the normalized variance indicates 11% variations of the actual potential around the equipotential. As shown in the figure, the fit deteriorates rapidly for bulk densities less than the best fit value and the waist ceases to be a gravitational low for bulk density <180 kg m^{-3}, which would invalidate the assumptions. This sets a lower limit on the density if our assumption of an equipotential is correct. The two lobes would be gravitationally bound to each other, with no strength required, even for densities down to 100 kg m^{-3}. The fit degrades much more slowly for higher values of density. Given the deviations from an equipotential, densities >220 kg m^{-3} are plausible but even 4× higher densities require moderate to high porosity of the bulk material for reasonable assumptions about the rock/ice ratio of the nucleus. The density is clearly in the range found for other, well studied comets such as Tempel 1 at 400 or 450 kg m^{-3} (*11, 48*), 81P/Wild 2 at 600 kg m^{-3} (*49*), and 19P/Borrelly at 240-490 kg m^{-3} (*50, 51*). All these determinations are model dependent and have large uncertainties but they are all consistent in being much less than the bulk density of pure ice.

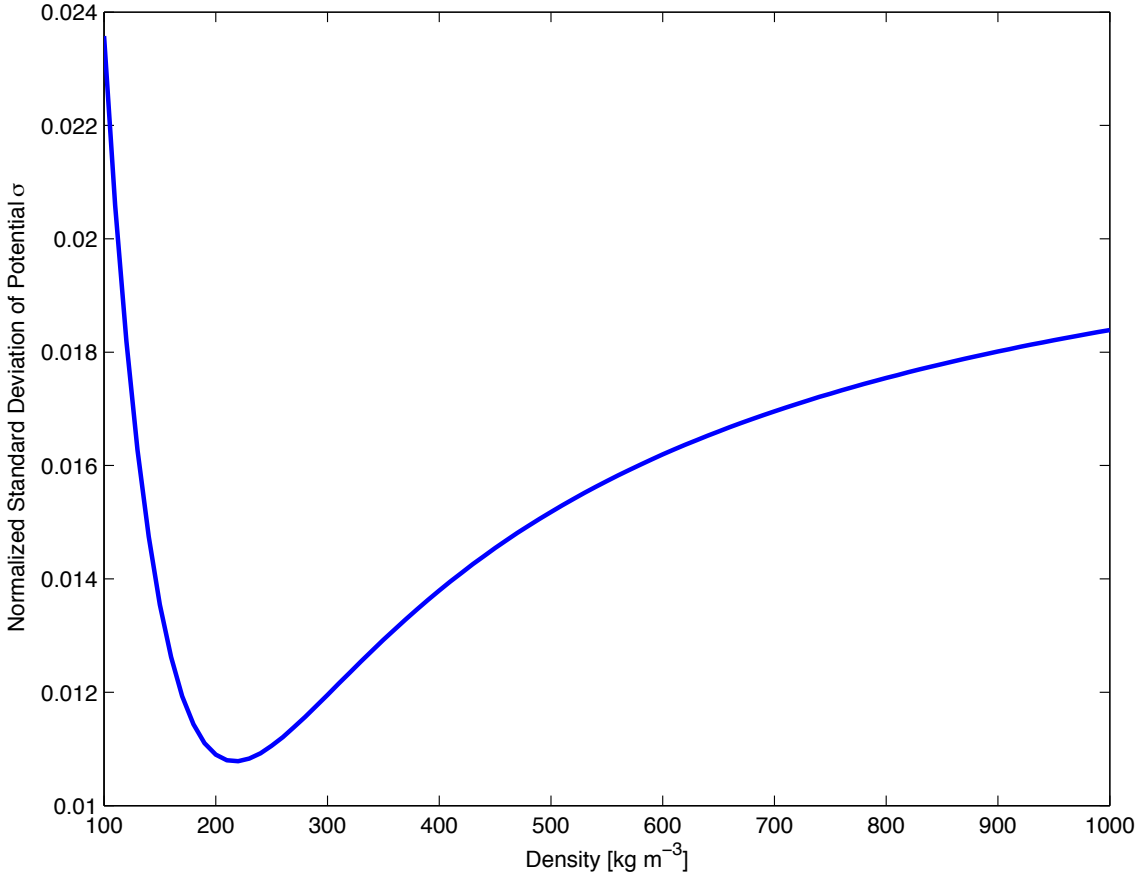

Figure S4. Variance of the potential fitted to the waist of Hartley 2 as a function of assumed density.

[1] The normalized variance is defined as $\sigma^2_{norm} = \frac{\Sigma A_i \left(U_i / U_A - 1 \right)^2}{\Sigma A_i}$ where A_i is the area of the i-th body surface element, U_i is the net potential of the i-th surface element, and $\underline{U_A}$ is the mean potential. It is thus a measure of the percentage deviations from the equipotential.

CN Anomaly

Routine imaging of the comet began on 5 Sep = E-60d, using primarily a clear filter sensitive to reflected light from grains in the coma and a narrow-band filter isolating an emission band of gaseous CN at 387 nm. The narrow band images were used to derive absolute gas and dust production rates of Hartley 2. To remove the continuum contribution in the CN filter, we assumed an unreddened solar continuum and convolved this with the filter transmission and quantum efficiency of the detector (*4*). The resulting CN fluxes were used to derive column densities using fluorescent efficiencies scaled to the comet's heliocentric distance and velocity (5*2*). To derive gas production rates, we compared the measured column densities to an image created from a Haser model (*53, 54*) with parent scale length 2×10^4 km & daughter scale length 2×10^5 km, values consistent with the expected lifetimes of HCN and CN against photodissociation. While the spatial distribution of CN released during the comet's regular activity can be described well with this Haser model, the spatial distribution of CN during the anomaly has a significantly shallower slope, suggesting an additional, extended source. A comparison of production of CN (Fig. S5) with the production of water (*15*) indicates that there was no corresponding increase in water release. A large amount of CN with little or no corresponding dust or water is quite surprising. The spatial profile of CN during the anomaly suggests that the CN was in grains too small or too dark to scatter much sunlight such as HCN polymers (*16*) or the CHON grains found at 1P/Halley (*17*). They would need to be lifted by something abundant and volatile. We do not yet have an appropriate physical model for the anomaly since the mechanism for producing the CN in the anomaly is apparently different from the one that operates normally.

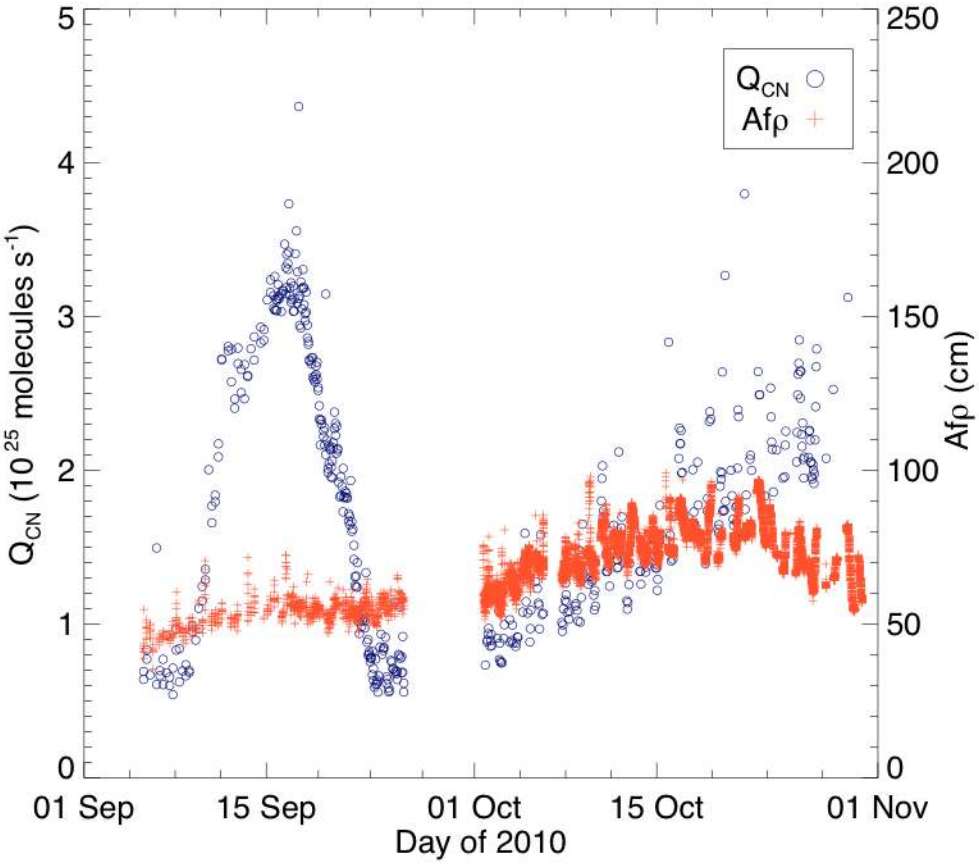

Figure S5. Temporal variation of CN and grain production. CN production in molecules/s compared with the production of grains measured by the parameter Afρ (*55*).

Discrete Chunks

The detailed size distributions and the spatial distributions of the large chunks are shown in Fig. S6 for a particular MRI image, mv5006001, taken ~1.5 minutes after closest approach**.** Fluxes were measured in several images in three ways: 1) by aperture photometry of each chunk in calibrated HRI images, 2) by aperture photometry of each chunk in deconvolved, calibrated HRI images, and 3) by fitting a point-spread function to individual chunks in calibrated MRI images. All three approaches lead to consistent results. Completeness was assessed by randomly inserting artificial sources of varying brightness and then finding them in the images using our automated routines. In the size distributions in Fig. S6 (upper two panels), points are plotted both as directly measured and after being corrected for incompleteness in recognizing chunks with our software. The same counting data are fitted separately to number as a function of measured flux (proportional to the cross-section of the chunk) and to number as a function of diameter (assuming Europa-like, icy scattering functions; *24, 25*). We also tried dirty scattering

functions based on the nucleus of comet Tempel 1 (*26*) but consider that less likely as discussed in the main text. Note that the chunks are distributed all around the nucleus without any prominent signs of discrete sources on the nucleus, suggesting that the motions of the grains have become isotropic in the nuclear frame due to the frequently varying gravitational field with every precession period.

With an expansion velocity upper-limit of 30 cm s^{-1}, we compute a mass-loss rate in the large chunks alone of 0.5 to 2 x 10^3 kg s^{-1}, but the uncertainties due to possible sublimation of icy grains and the unknown density of aggregates could alter this number substantially.

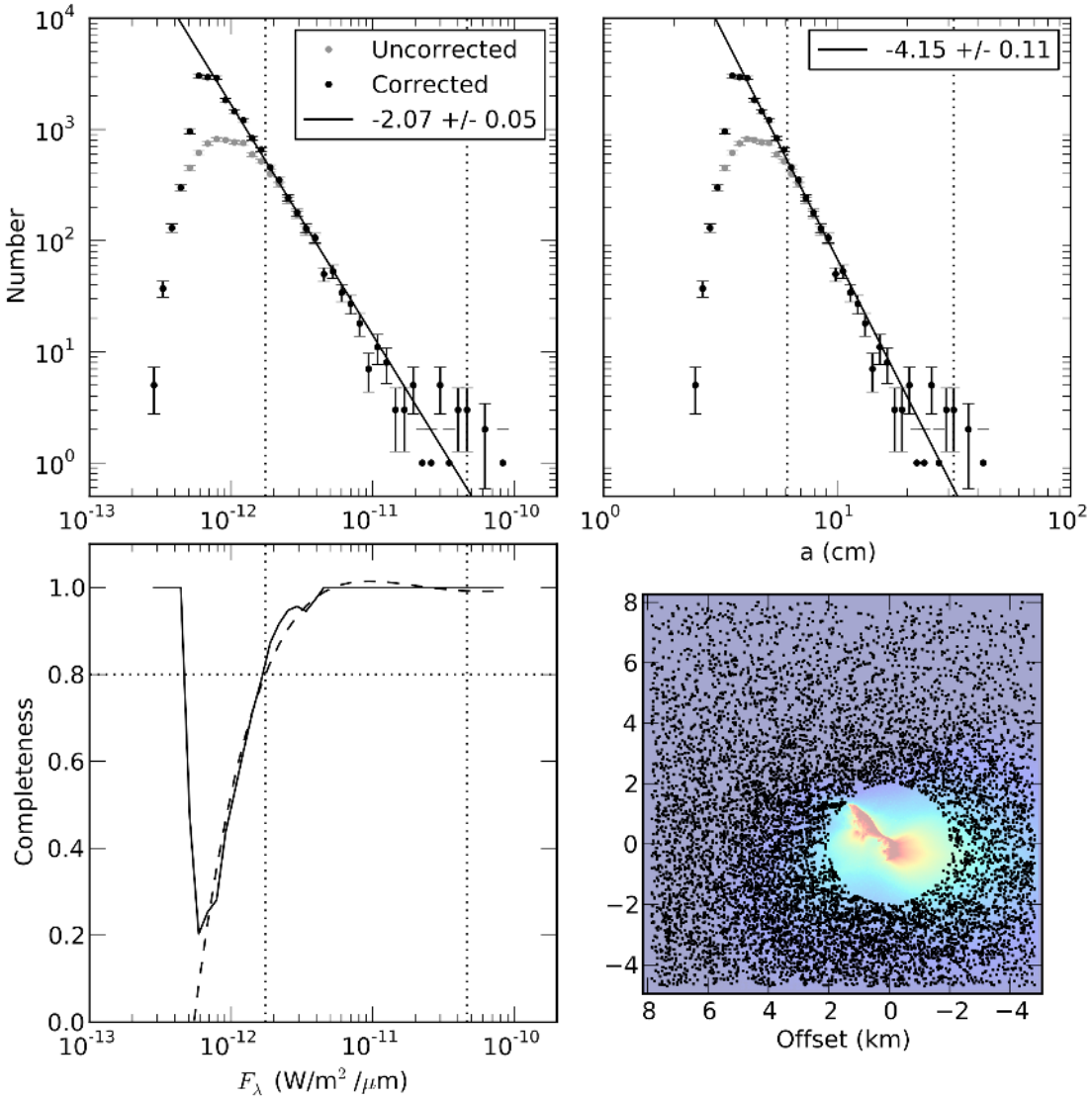

Figure S6. Distribution of chunks seen in MRI image mv5006001. The image was taken 1.5 min after closest approach. Upper left shows the distribution as a function of measured flux from each chunk [W m^{-2} μm^{-1}] while the upper right shows the distribution as a function of

diameter [cm] assuming icy chunks. The lower left is an empirical test of the completeness of our counting as a function of the observed flux and is used to correct the actual data in the upper plots. The lower right shows a map of the spatial distribution of the particles in this image with sun at the right.

Spectral Maps

Spectral processing for each long-slit spectrum includes: a) removal of instrumental thermal background that depends strongly on known quantities such as temperatures inside the spectrometer but also when the most recent previous spectrum was taken and sometimes on the signal in the last previous spectrum; b) correction for non-linearity in the gain of the spectrometer; c) conversion to radiance. Extraction of spectra includes allowance for curvature of the slit as imaged onto the detector (commonly known as spectral "smile"), summing or averaging over spatial pixels both along the slit and from one spectrum to another during a scan. For most purposes, more useful spectra are then obtained by subtracting the continuum, which consists of reflected sunlight at the shorter wavelengths and thermal emission at the longer wavelengths. For the spectra presented in this paper, the continuum has been removed by linearly interpolating between segments of the spectrum thought to be representative of the continuum (reflected sunlight). When only absorption features are of interest, the spectrum is divided by the solar spectrum before subtracting the continuum but this step is omitted when the fluxes of emission features are also of interest. Eventually a proper thermal and scattering model will be used to remove the continuum but this is a major task. From past experience we have limited our conclusions here to ones that will not be affected by improvements to the processing.

Figure 5 was from a spectral scan centered at E+7min consisting of 56 spectra taken over ~2.5 minutes with an exposure time of 1.4 sec per frame during a continuous scan at 1 slit-width per frame. The scan will be available in the PDS archive as image id hi5006000. The maps shown are integrated over the relevant spectral range. A mask was used to suppress the nucleus. The maps have a scale of 52 m/pixel; the maps of the gases are smoothed with a 3x3-pixel box but the map of the ice is not smoothed. All maps are linear in intensity but with varying amounts of stretch. The stretch in the images is best understood by looking at the actual spectra in Fig. 6. Those spectra are averages of the surface brightness (radiance) over the boxes and were reduced from the calibrated radiance spectra by fitting straight lines to portions of the spectrum thought to be true continuum. Radiances integrated over the emission bands in the two boxes are: Water-rich waist: $B(H_2O) = 1.7\times10^{-3}$, $B(CO_2) = 4.1\times10^{-4}$, and Ice-rich lobe: $B(H_2O) = 1.1\times10^{-3}$, $B(CO_2) = 8.1\times10^{-4}$, all in [W m^{-2} sr^{-1}]. At this stage of processing, the spectral profile of the organic emission is not yet reliable due to difficulty in separating the ice absorption, the smooth reflected continuum, and the thermal emission, all of which matter at the wavelength of the organics. Because these factors vary from pixel to pixel, the uncertainties in the map of organics are much larger than the uncertainties in the maps of the strong emission features of H_2O and CO_2. Based on abundances reported from remote sensing, we presume that the emission is dominated by gaseous methanol (CH_3OH), but further discussion of the organic emission is premature.

In order to study the icy grains further, we have calculated models for the reflection spectrum using the optical constants of ice (*56*) and compared them with the relative reflectance spectrum in Fig. S7. The observed spectrum is the same as the one for the ice-rich region in Fig. 6, but processed to relative reflectance. In this case, the thermal emission was subtracted from the observed spectrum as an empirically fit Planck function and the result was divided by the solar spectrum so that any residual "color" due to the scattering properties would remain. It was then normalized at 1.8 μm. The model spectra (*57*) are for solid spheres of pure, hexagonal ice in an areal mixture with particles assumed to have a reddish slope, characteristic of refractory grains in comets, *i.e.*, the sum of a reddish continuum and a theoretical ice spectrum. The best fit is sensitive to the sizes of the particles but a range of mixing ratios and slopes for the reddish material provides nearly equivalent fits. Archival ID for the data is hi5006000.

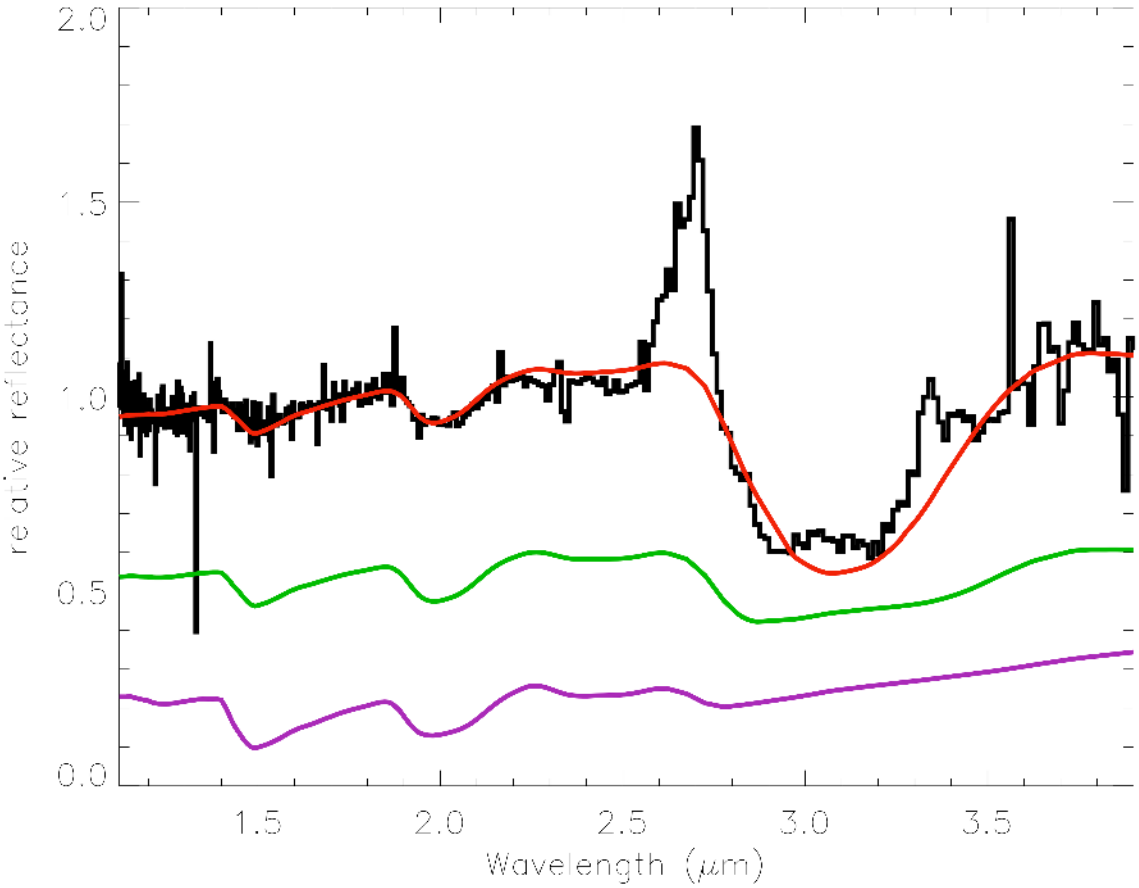

Figure S7 Relative reflectance spectrum of the coma. The smooth curves are theoretical spectra of icy grains of 1 (red), 10 (green), and 100 (purple) μm diameter, normalized to unity at 1.8 μm. The latter two curves have been displaced vertically for clarity. The variation in relative strength of the absorption features at 1.5, 2.0, and 3.2 μm shows that the dominant size of the ice must be less than a few μm.

The fits to the relative reflectance spectrum are primarily sensitive to the size of the icy particles and it is clear that the dominant source of scattered light from the ice must be particles with diameters less than 10μm. This is consistent with the earlier conclusion

that the dominant source of light must be the smallest particles, no matter what the large chunks are. We note that large fluffy aggregates can mimic individual grains of the same size as the constituent pieces of the aggregate and can thus appear small in this type of analysis, even though the actual, porous particles may be much larger. This result is very similar to the result obtained at Tempel 1 after the impact (no ice was observed prior to the impact). Those grains, which had undergone an excavating shock, were predominantly micron-sized (*27*). The similarity between excavated material from Tempel 1 and ambient outgassing from Hartley 2 suggests that the constituent solid grains of ice are of order a micron in most comets and that the icy grains seen at Hartley 2 are also from the subsurface.

The spectral map made at E-55 hr was taken from spectral scan hi4000039, integrated over areas of 120×120 km and 600×600 km, centered on the nuclear position (defined by the peak thermal emission) to produce the spectra in Fig. S8. The continuum was determined manually and interpolated with straight lines. The interpolation uncertainties could allow some absorption by ice in the 3-μm band, which would imply a higher total production of water vapor than deduced from these spectra. The band ratio of CO_2/H_2O differs between the two spectra indicating that the optical depth of the bands is still affecting the result in the 120-km box. Average column densities based on an optically thin assumption are: 120-km: $N(H_2O) = 6.2\times10^{15}$ cm^{-2}, $N(CO_2) = 8.4\times10^{14}$ cm^{-2}; 600-km: $N(H_2O) = 1.7\times10^{15}$ cm^{-2}, $N(CO_2) = 3.2\times10^{14}$ cm^{-2}. For simple, radial outflow, the average column density should be inversely proportional to the size of box, but this can be altered either by an extended source of H_2O from the icy grains or by significant optical depth of either species in the 120-km box. For assessing the total release of volatiles, the 600-km box is the better choice.

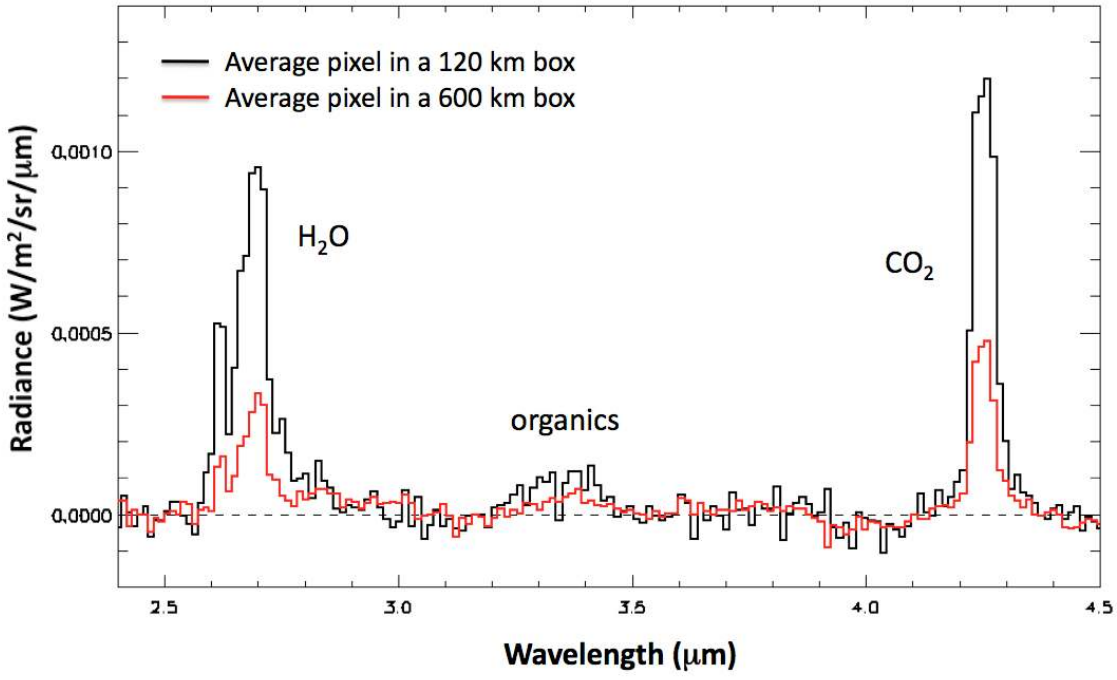

Figure S8. Continuum-removed spectra of Hartley 2 taken 55 hours before closest approach.

The spectra used in Fig. 7 were from a large number of short, spatial scans taken at a rapid cadence on departure, hi4300007 through hi4500017. To ensure coverage of the comet by short scans, the rate was set to two slit widths per frame rather than the more usual one slit width per frame. Thus a square box of 5×5 pixels was used to extract the flux but this actually corresponds to a 10×5 pixel field of view. The range was changing during the period of the scans so the size of the box is not constant in km but is roughly 350×175 km, large enough that the effects of optical depth are minimized.

References and Notes

1. M. F. A'Hearn *et al*., Deep Impact: excavating comet Tempel 1. *Science* **310**, 258 (2005). doi:10.1126/science.1118923 Medline

2. M. F. A'Hearn, M. R. Combi, Eds., *Icarus* **191**, 1 (2007).

3. D. L. Hampton *et al*., An overview of the instrument suite for the Deep Impact mission. *Space Sci. Rev.* **117**, 43 (2005). doi:10.1007/s11214-005-3390-8

4. K. P. Klaasen *et al*., Invited article: Deep Impact instrument calibration. *Rev. Sci. Instrum.* **79**, 091301 (2008). doi:10.1063/1.2972112 Medline

5. O. Groussin, P. Lamy, L. Jorda, I. Toth, The nuclei of comets 126P/IRAS and 103P/Hartley 2. *Astron. Astrophys.* **419**, 375 (2004). doi:10.1051/0004-6361:20040073

6. C. M. Lisse *et al*., Spitzer Space Telescope observations of the nucleus of Comet 103P/Hartley 2. *Publ. Astron. Soc. Pac.* **121**, 968 (2009). doi:10.1086/605546

7. L. A. Soderblom *et al*., Observations of comet 19P/Borrelly by the miniature integrated camera and spectrometer aboard Deep Space 1. *Science* **296**, 1087 (2002). doi:10.1126/science.1069527 Medline

8. A. Fujiwara *et al*., The rubble-pile asteroid Itokawa as observed by Hayabusa. *Science* **312**, 1330 (2006). doi:10.1126/science.1125841 Medline

9. M. J. S. Belton, J. Melosh, Fluidization and multiphase transport of particulate cometary material as an explanation of the smooth terrains and repetitive outbursts on 9P/Tempel 1. *Icarus* **200**, 280 (2009). doi:10.1016/j.icarus.2008.11.012

10. M. S. Robinson, P. C. Thomas, J. Veverka, S. Murchie, B. Carcich, The nature of ponded deposits on Eros. *Nature* **413**, 396 (2001). doi:10.1038/35096518 Medline

11. J. E. Richardson, H. Melosh, C. Lisse, B. Carcich, A ballistics analysis of the Deep Impact ejecta plume: Determining Comet Tempel 1's gravity, mass, and density. *Icarus* **190**, 357 (2007). doi:10.1016/j.icarus.2007.08.001

12. H. U. Keller *et al*., *Astron. Astrophys.* **187**, 107 (1987).

13. D. E. Brownlee *et al*., Surface of young Jupiter family comet 81P/Wild 2: View from the Stardust Spacecraft. *Science* **304**, 1764 (2004). doi:10.1126/science.1097899 Medline

14. P. C. Thomas *et al*., The shape, topography, and geology of Tempel 1 from Deep Impact observations. *Icarus* **187**, 4 (2007). doi:10.1016/j.icarus.2006.12.013

15. M. R. Combi *et al*., *Astrophys. J.* **734**, L6 (2011).

16. C. N. Matthews, R. Ludicky, Hydrogen cyanide polymers on comets. *Adv. Space Res.* **12**, 21 (1992). doi:10.1016/0273-1177(92)90149-R Medline

17. J. Kissel *et al*., Composition of comet Halley dust particles from Giotto observations. *Nature* **321**, (6067s), 336 (1986). doi:10.1038/321336a0

18. J. K. Harmon *et al.*, *IAU Circ.* **9179**, 1 (2010).

19. J. K. Harmon *et al.*, *Astrophys. J.* **734**, L2 (2011).

20. J. K. Harmon *et al.*, in *Comets II*, M. C. Festou *et al.*, Eds. (Univ. Arizona Press, Tucson, 2005), p. 274.

21. M. F. A'Hearn, E. Dwek, A. T. Tokunaga, Where is the ice in comets. *Astrophys. J.* **248**, L147 (1981). doi:10.1086/183644

22. H. Campins, G. H. Rieke, M. J. Lebofsky, Ice in Comet Bowell. *Nature* **301**, 405 (1983). doi:10.1038/301405a0

23. M. S. Hanner, Comet Cernis—Icy grains at last? *Astrophys. J.* **277**, L78 (1984). doi:10.1086/184207

24. W. M. Grundy *et al.*, New Horizons Team, New horizons mapping of Europa and Ganymede. *Science* **318**, 234 (2007). doi:10.1126/science.1147623 Medline

25. B. Buratti, J. Veverka, Voyager photometry of Europa. *Icarus* **55**, 93 (1984). doi:10.1016/0019-1035(83)90053-2

26. J.-Y. Li *et al.*, Deep Impact photometry of Comet 9P/Tempel 1. *Icarus* **187**, 141 (2007). doi:10.1016/j.icarus.2006.09.018

27. J. M. Sunshine *et al.*, The distribution of water ice in the interior of Comet Tempel 1. *Icarus* **190**, 284 (2007). doi:10.1016/j.icarus.2007.04.024

28. H. Patashnick, G. Rupprecht, The lifetime of ice particles in the solar system. *Icarus* **30**, 402 (1977). doi:10.1016/0019-1035(77)90174-9

29. M. S. Hanner, On the dectectability of icy grains in the comae of comets. *Icarus* **47**, 342 (1981). doi:10.1016/0019-1035(81)90182-2

30. H. I. M. Lichtenegger, N. I. Kömle, Heating and evaporation of Icy particles in the vicinity of comets. *Icarus* **90**, 319 (1991). doi:10.1016/0019-1035(91)90110-F

31. H. A. Weaver *et al.*, Detection of CO Cameron band emission in comet P/Hartley 2 (1991 XV) with the Hubble Space Telescope. *Astrophys. J.* **422**, 374 (1994). doi:10.1086/173732

32. L. Colangeli *et al.*, *Astron. Astrophys.* **343**, L87 (1999).

33. J. Crovisier *et al.*, *ESA SP* **427**, 161 (1999).

34. L. M. Feaga, M. Ahearn, J. Sunshine, O. Groussin, T. Farnham, Asymmetries in the distribution of H_2O and CO_2 in the inner coma of Comet 9P/Tempel 1 as observed by Deep Impact. *Icarus* **190**, 345 (2007). doi:10.1016/j.icarus.2007.04.009

35. H. A. Weaver *et al.*, *Astrophys. J.* **734**, L5 (2011).

36. L. M. Feaga *et al.*, *Bull. Amer. Astron. Soc.* **38**, 450 (2007).

37. D. Bockelée-Morvan *et al.*, in *Comets II*, M. C. Festou *et al.*, Eds. (Univ. Arizona Press, Tucson, 2005), p. 391.

38. M. J. S. Belton, in *Comets in the Post-Halley Era*, vol. 2, R. L. Newburn *et al.*, Eds. (Kluwer, Dordrecht, 1991) p. 697.

39. N. H. Samarasinha, M. F. A'Hearn, Observational and dynamical constraints on the rotation of Comet P/Halley. *Icarus* **93**, 194 (1991). doi:10.1016/0019-1035(91)90208-B

40. N. H. Samarasinha *et al.*, in *Comets II*, M. C. Festou *et al.*, Eds. (Univ. Arizona Press, Tucson, 2005), p. 281.

41. M. J. S. Belton *et al.*, *Icarus* **231**, 345 (2011).

42. K. J. Meech *et al.*, *IAU Circ.* **9163**, 1 (2010).

43. N. H. Samarasinha *et al.*, *IAU Circ.* **9178**, 1 (2010).

44. E. Jehin *et al.*, *CBET* **2589**, 1 (2010).

45. M. Knight, D. Schleicher, *IAU Circ.* **9163**, 1 (2010).

46. M. J. S. Belton *et al.*, The spin state and homogeneity of comet Halley's nucleus. *Icarus* **95**, 183 (1991). doi:10.1016/0019-1035(91)90207-A

47. N. H. Samarasinha, M. J. S. Belton, Long-Term Evolution of Rotational States and Nongravitational Effects for Halley-like Cometary Nuclei. *Icarus* **116**, 340 (1995). doi:10.1006/icar.1995.1129

48. B. J. R. Davidsson, P. J. Gutiérrez, H. Rickman, Nucleus properties of Comet 9P/Tempel 1 estimated from non-gravitational force modeling. *Icarus* **187**, 306 (2007). doi:10.1016/j.icarus.2006.07.022

49. B. J. R. Davidsson, P. J. Gutiérrez, Non-gravitational force modeling of Comet 81P/Wild 2I. A nucleus bulk density estimate. *Icarus* **180**, 224 (2006). doi:10.1016/j.icarus.2005.07.023

50. B. J. R. Davidsson, P. J. Gutiérrez, Estimating the nucleus density of Comet 19P/Borrelly. *Icarus* **168**, 392 (2004). doi:10.1016/j.icarus.2003.11.009

51. T. L. Farnham, A. L. Cochran, A McDonald Observatory study of Comet 19P/Borrelly: Placing the Deep Space 1 observations into a broader context. *Icarus* **160**, 398 (2002). doi:10.1006/icar.2002.6969

52. D. G. Schleicher, The fluorescence efficiencies of the CN violet bands in comets. *Astron. J.* **140**, 973 (2010). doi:10.1088/0004-6256/140/4/973

53. L. Haser, *Bull. Cl. Sci. Acad. R. Liege* **43**, 740 (1957).

54. M. C. Festou, *Astron. Astrophys.* **95**, 69 (1984).

55. M. F. A'Hearn, D. G. Schleicher, R. L. Millis, P. D. Feldman, D. T. Thompson, Comet Bowell 1980b. *Astron. J.* **89**, 579 (1984). doi:10.1086/113552

56. S. G. Warren, R. E. Brandt, Optical constants of ice from the ultraviolet to the microwave: A revised compilation. *J. Geophys. Res.* **113**, (D14), D14220 (2008). doi:10.1029/2007JD009744

57. B. Hapke, *Theory of Reflectance and Emittance Spectroscopy* (Cambridge Univ. Press, Cambridge, UK, 1993).

Acknowledgment: Data from EPOXI will be released through NASA's Planetary Data System in 2011. Image IDs in this paper are part of the final ID in the archive. This was

supported by NASA's Discovery Program contract NNM07AA99C to the University of Maryland and task order NMO711002 to the Jet Propulsion Laboratory. The work was supported by the home institutions of several of the scientists, particularly by the University of Maryland. The contributions of O. Groussin and F. Merlin to this project were funded in part by the Centre National d'Etudes Spatiales (CNES).